ACS Catalysis

Open Access
This article is licensed under CC-BY 4.0

pubs.acs.org/acscatalysis
Research Article

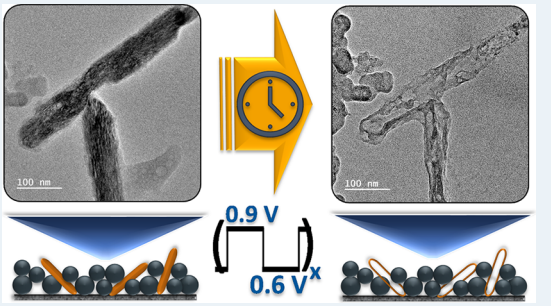
Durability Assessment of α-MnO_2 Nanorods for Alkaline ORR under Application-Relevant Conditions

Alexander Rampf,* Vincent Martin, Michal Ronovský, Andres O. Godoy, Thomas Diemant, Frédéric Maillard, Kavita Kumar,* Marian Chatenet, and Roswitha Zeis

Cite This: https://doi.org/10.1021/acscatal.6c06787
Read Online

ACCESS | Metrics & More | Article Recommendations | Supporting Information

ABSTRACT: This study investigates the durability of α-MnO_2, one of the most cost-effective catalysts for the oxygen reduction reaction (ORR) in alkaline media. A comprehensive set of various characterization techniques, including identical location transmission electron microscopy (IL-TEM), differential electrochemical mass spectrometry (DEMS), rotating ring-disk electrode (RRDE), and online inductively coupled plasma mass spectrometry (ICP-MS) coupled to both flow cell and gas diffusion electrode (GDE) half-cell, was employed. In addition, accelerated stress test (AST) measurements in the GDE half-cell followed by *post mortem* X-ray photoelectron spectroscopy (XPS), synchrotron X-ray diffraction (XRD), scanning electron microscopy (SEM), and TEM analysis were performed. Three electrolyte and temperature combinations ranging from standard lab conditions to application-relevant conditions were systematically investigated. The results reveal that Mn dissolution occurs under oxygen-free conditions due to oxidation-state transitions of the catalyst, whereas under oxygen, it is further accelerated by degradation processes associated with peroxide formation as a byproduct of the ORR, particularly at higher ORR overpotentials. Both increasing KOH concentration and temperature significantly enhance Mn dissolution due to accelerated Mn reduction and dissolution kinetics. Despite the increased dissolution, the condition of 4.0 M KOH at 25 °C exhibits the highest ORR activity after 5000 AST cycles. This apparent discrepancy is attributed to surface roughening of the catalyst, leading to an increased electrochemically active surface area. Overall, the results demonstrate that α-MnO_2 exhibits promising initial ORR activity but undergoes substantial Mn dissolution under operating conditions. These findings provide mitigation strategies to limit catalyst degradation and improve operational durability.



KEYWORDS: *manganese dioxide, oxygen reduction reaction (ORR), accelerated stress test (AST), online inductively coupled plasma mass spectrometry (online ICP-MS), identical location transmission electron microscopy (IL-TEM), differential electrochemical mass spectrometry (DEMS), gas diffusion electrode (GDE) half-cell*

1. INTRODUCTION

Manganese dioxide is widely used in various energy-related applications.[1,2] Among them, it has been used for decades as the positive electrode material in commercial metal-air batteries, especially in zinc-air batteries.[3] Compared to the conventionally employed oxygen reduction reaction (ORR) catalysts Pt and Ag, manganese dioxide offers several advantages, including low cost, high and widespread natural abundance, and considerable ORR activity in alkaline media.[4,5]

Among the manganese dioxide polymorphs, α-MnO_2 exhibits the highest ORR activity, which is attributed to its distinctive crystal structure.[4,6] Similarly, δ-MnO_2 (birnessite), which possesses a layered crystal structure, has also been reported to exhibit comparable ORR activity in some studies.[7] α-MnO_2 possesses one of the most open frameworks with (2 × 2) crystal tunnels, enabling enhanced ion diffusion and thus facilitating adsorption.[8] In addition, the open structure facilitates proton insertion, which is essential to create Mn^{III} defects substituting Mn^{IV} sites.[9] These Mn^{III} species are widely regarded as catalytically active sites in α-MnO_2.[9−11] The Mn^{III} species has only one unpaired electron on the e_g orbital and therefore shows enhanced O_2 adsorption energies, thereby improving ORR kinetics.[12,13] Furthermore, we have recently demonstrated that the primary limitation of α-MnO_2, its inherent low electronic conductivity, can be mitigated by tuning the α-MnO_2-to-carbon ratio in the catalyst layer. When combined with optimized α-MnO_2 loadings, this strategy enables alkaline ORR performance approaching that of Pt-based electrodes.[14]

Received: August 21, 2026
Revised: October 10, 2026
Accepted: October 14, 2026

Downloaded from pubs.acs.org/acscacs/article-pdf/doi/10.1021/acscatal.6c06787/6916174/cs-2026-06787e.pdf by KIT BIBLIOTHEK user on 16 November 2026

© XXXX The Author(s). Published by American Chemical Society

Moreover, the ORR can occur in different pathways, with the four-electron pathway being desirable because it avoids the formation of potentially corrosive peroxide species associated with the two-electron pathway and maximizes the energy efficiency of the resulting device.

However, an ideal catalyst must not only exhibit high activity via a four-electron pathway but also demonstrate sufficient durability. Because applying realistic operating potentials over the estimated full lifetime of a device is highly time-consuming, accelerated stress tests (ASTs), also referred to as accelerated durability tests (ADTs), have been developed. One of the early standardized AST protocols was proposed by Ohma et al.,[15] who aimed to harmonize testing procedures for fuel cells and corresponding half-cells for automotive applications. Their protocol includes rectangular potential cycles between 0.6 and 1.0 V vs RHE (3 s hold at each potential) to simulate load cycling, combined with intermittent triangular cycles between 1.0 and 1.5 V vs RHE to mimic start-stop events. Since start-stop events are not relevant for metal-air batteries, the present study focuses exclusively on load cycling. Furthermore, the upper potential limit (UPL) was reduced from 1.0 to 0.9 V vs RHE, as the open-circuit potential of α-MnO_2 is 107 mV lower than that of Pt-based electrodes.[14] This reduction in the UPL is also relevant for evaluating the stability of α-MnO_2 while avoiding potential contributions from carbon corrosion, which starts at potentials around 1.0 V vs RHE.[16]

Although previous studies have primarily investigated the durability of manganese dioxide using rotating disk electrodes,[17,18] durability studies employing a gas diffusion electrode (GDE) half-cell setup remain scarce.[19−22] Such a configuration allows catalyst stability evaluation under more realistic operating conditions, including higher current densities, elevated alkaline electrolyte concentrations, and the presence of a triple-phase boundary, as encountered in practical devices. These parameters can strongly influence catalyst degradation and therefore provide a more technically relevant durability assessment.[23,24] Accordingly, in this study, the ASTs were also conducted with a GDE half-cell. In addition, measurements were performed under both argon and oxygen conditions, as the presence of oxygen can substantially alter degradation mechanisms compared to oxygen-free conditions.[18,25]

By employing a broad range of complementary characterization techniques, we gain deeper insight into the durability of α-MnO_2 during the ORR. Identical location transmission electron microscopy (IL-TEM) is used to analyze morphological changes occurring during the ORR, while inductively coupled plasma mass spectrometry (ICP-MS) measurements coupled to the flow cell and the GDE half-cell provide mechanistic insight and enable quantification of dissolved Mn species. In addition, AST measurements in the GDE half-cell reveal the ORR performance degradation of α-MnO_2-based electrodes under various conditions. These investigations are further complemented by differential electrochemical mass spectrometry (DEMS) as well as *post mortem* XPS, synchrotron XRD, TEM, and SEM analyses. Through this holistic approach, we seek to achieve a more comprehensive understanding of the degradation processes of α-MnO_2.

2. METHODS

All chemicals in this work were used as received without further purification. Ultrapure water (18.2 MΩ) was used for the syntheses, preparing the KOH solutions, and cleaning. All potentials in this study are given against the reversible hydrogen electrode (RHE).

2.1. Electrocatalyst, Inks, and Gas Diffusion Electrodes

The synthesis of α-MnO_2 was performed following the procedure reported in our previous work.[14] The ink for the GDE was prepared by dispersing the synthesized α-MnO_2 and Vulcan-XC-72R (FuelCellStore) in a 1:1 solution of ultrapure water and isopropanol. The mixture was homogenized in an ultrasonic bath for about 30 min, after which a respective amount of a 60 wt % polytetrafluoroethylene (PTFE) dispersion in water (Sigma-Aldrich) was added. The ink was subsequently homogenized again and transferred to a spray-coating system (Exactacoat, Sono-Tek, equipped with a 120 kHz impact nozzle). The coating was made on a gas diffusion layer (GDL) with a microporous layer (MPL, Freudenberg H23 C2), which was placed on a vacuum and heating plate set at 80 °C. The flow rate was set to 0.1 mL min^{-1}, the *x* and *y* nozzle speeds were fixed at 20 mm s^{-1}, and the power was set to 3 W. The resulting dry electrode consisted of 20% α-MnO_2 supported on Vulcan with 5 wt % PTFE in the catalyst layer. The α-MnO_2 loading was fixed at 50 μg cm^{-2}.

2.2. Identical Location Transmission Electron Microscopy (IL-TEM)

IL-TEM and *post mortem* TEM analyses were performed using a JEOL 2010 TEM instrument operated at 200 kV with a point-to-point resolution of 0.19 nm (LaB_6 filament). The catalyst was drop-cast onto an Au lacey carbon grid (300 mesh, Ted Pella) for the IL-TEM analyses from an ink containing 20% α-MnO_2/C and Nafion D2020 dispersion. For *post mortem* TEM analysis, catalyst material was scraped from the GDE after AST and deposited onto a Cu lacey carbon grid (200 mesh, Ted Pella). Electrochemical IL-TEM measurements were conducted using an Autolab potentiostat (VIONIC, Metrohm) in a temperature-controlled, in-house-built cell filled with KOH electrolyte (Sigma-Aldrich). Prior to the experiment, the glassware, PTFE-based material, and electrodes were cleaned using 50% v/v solution of H_2O_2 (Carl Roth, 30 wt %) and H_2SO_4 (Merck, 96 wt %), and rinsed three times with ultrapure water. ASTs were performed by applying alternating potential steps of 0.9 and 0.6 V vs RHE, each held for 3 s, with the TEM grid serving as the working electrode. A glassy carbon disk and an RHE (HydroFlex, Gaskatel) were used as the counter and reference electrodes, respectively. The electrolyte was continuously purged with oxygen during the measurements to ensure full saturation. The IL-TEM images were acquired from identical regions of the TEM grid before and after AST using Gatan Microscopy Suite software. The procedure for calculating the interplanar spacing is provided in the Supporting Information (*cf.* Figure S1 and accompanying text).

2.3. Inductively Coupled Plasma Mass Spectrometry (ICP-MS)

An Autolab potentiostat (PGSTAT302N) and a custom-designed ICP-MS flow cell, as previously described,[26,27] were used to conduct the experiments. A PerkinElmer NexION 2000c spectrometer was used as ICP-MS instrument. The working electrode was a glassy carbon disk (5 mm diameter) embedded in polychlorotrifluoroethylene (PCTFE) material. The catalyst was deposited onto the working electrode by drop-casting 10 μL of the ultrasonically homogenized suspension, resulting in a loading of 10 μg_{MnO_2} cm^{-2}. A glassy carbon rod (SIGRADUR® grade G, HTW), positioned upstream of the electrolyte flow, served as the counter electrode, while a commercial RHE (mini-HydroFlex, Gaskatel) was used as the reference electrode. Ar- or O_2-saturated 0.1 M KOH (Sigma-Aldrich) (Ar 5.0 > 99.999%, O_2 5.0 > 99.999%, Messer) was continuously flowed through the cell, which had a volume of about 70 μL. There was a constant flow rate toward the ICP-MS of 206 ± 7 μL min^{-1} and 213 ± 3 μL min^{-1} from the flow cell and the GDE half-cell, respectively. The exact flow rate was determined at the end of each experiment.

Downloaded from pubs.acs.org/acscatal/article-pdf/doi/10.1021/acscatal.6c06787/6916174/cs-2026-06787e.pdf by KIT BIBLIOTHEK user on 16 November 2026

https://doi.org/10.1021/acscatal.6c06787
ACS Catal. XXXX, XXX, XXX−XXX

GDE half-cell online ICP-MS measurements were conducted following a similar approach. A modified GDE half-cell (Flexcell® PTFE, Gaskatel) equipped with a capillary positioned at the center of the GDE was employed, with the capillary at the other end directly connected via a *y*-connector to the ICP-MS. The other opening of the *y*-connector was connected to the internal standard (Rh, 10 ppb, Carl Roth) solution in 2 wt % HNO_3 (Suprapur, Onlinecas), in order to correct the spectrometer deviation during long-term tests and acidify the alkaline electrolyte. To maintain a constant electrolyte volume during operation, fresh electrolyte was continuously supplied to the GDE half-cell at a flow rate matching that of the electrolyte withdrawn for ICP-MS analysis. The cell was initially filled with 30 mL of 0.1 M KOH. During the measurement, the cell was purged with either Ar or O_2. For each experiment, the collection efficiency was calculated and taken into account when determining the amount of dissolved Mn. Detailed information on the calculation of the collection efficiency is provided in the Supporting Information.

All experiments were conducted at 22 ± 2 °C. Calibration curves were established using Mn standard solutions with concentrations of 0, 5, 10, and 20 μg L^{-1}. These standards were freshly prepared by diluting a mono-element ICP standard solution (1000 mg L^{-1}, Carl Roth GmbH) with 0.1 mol L^{-1} KOH solution, completed by 2 wt % HNO_3 solution. For each concentration, 100 μL of pure HNO_3 was added to stabilize the dissolved Mn. Calibration measurements were performed before and after each experiment, with deviations found to be less than 5%. Signals for ^{55}Mn were recorded in standard mode. Subsequent to each experiment, a potential pulse was applied to the working electrode, producing a high-intensity ICP-MS signal. This signal was used to determine the delay time ($t < 8$ s for flow cell, and $t < 20$ s for GDE half-cell) required to synchronize the Autolab potentiostat data with the ICP-MS signal. ICP-MS data were acquired with a dwell time of 100 ms, ensuring a high signal-to-noise ratio and an optimal analysis frequency. The electrochemical measurements were performed with 80% in situ iR-drop correction and an additional 20% post correction. For the oxygen measurements in the GDE half-cell, a 100% iR post correction was applied. The error bars of the integrated dissolution amount are based on the standard deviation of at least two independent measurements.

2.4. Differential Electrochemical Mass Spectrometry (DEMS)

Cyclic voltammetry coupled to mass spectrometry was performed using a VMP2Z potentiostat in an in-house-built spectroelectrochemical cell filled with 0.1 M KOH (Sigma-Aldrich). The cell was physically separated from the mass spectrometer (QME 220, Pfeiffer Vacuum) by a porous stainless-steel frit supporting three layers of porous hydrophobic PTFE membranes (Cobetter filtration; 20 μm thickness, 20 nm pore diameter, 10 mm diameter) to ensure water tightness. The working electrode consisted of a ca. 50 nm thick sputter-coated gold film (the current collector) deposited on the PTFE membrane, onto which the catalyst, either 20% α-MnO_2/C or Vulcan XC-72R, was applied by drop-casting. The α-MnO_2 loading was ca. 30 μg cm^{-2}. Measurements with Vulcan alone were performed as background experiments using the same Vulcan loading as in the 20% α-MnO_2/C measurement. A platinum grid (2 cm^2) served as the counter electrode, and an RHE (HydroFlex, Gaskatel) was used as the reference electrode. Gaseous species generated at the surface of the WE during CV were extracted through the PTFE membranes and steel frit by a vacuum cascade (via the vacuum chamber design with two turbomolecular pumps - HiPace300, Pfeiffer Vacuum) and subsequently directed to the mass spectrometer. Ion currents of selected species were recorded sequentially, with the acquisition time for each species optimized to ensure reliable detection while maintaining adequate temporal resolution relative to the CV scan rate of 50 mV s^{-1}.

2.5. GDE Half-Cell Measurements

The GDEs were tested in a commercial GDE half-cell (Flexcell® PTFE, Gaskatel) with a VMP-3e potentiostat (Biologic) in KOH electrolyte (Sigma-Aldrich). The geometrical active surface area was fixed to 0.5 cm^2 by gaskets. An RHE (Mini-HydroFlex, Gakatel) served as reference electrode, while a Ti/Ir mixed oxide grid (METAKEM) was used as the counter electrode. The cell was heated to 25 °C or 50 °C using PTC heating elements connected to a temperature control box (Gaskatel). Before starting a measurement, the cell was purged with oxygen for 45 min. Polarization curves and ASTs were conducted while aiming for iR-free potentials between 0.6 V vs RHE and open-circuit potential (OCP). Details of the polarization curve measurement protocol are provided in the Supporting Information (*cf.* Figure S2 and accompanying text). ASTs were performed between the polarization curves using alternating current steps of −0.01 mA cm^{-2} and the maximum current used for the polarization curve, each applied for 3 seconds. For each experimental condition, two independent measurements were carried out using two separate electrodes. Error bars represent the standard deviation of these measurements. For the final polarization curve in Figure 5c, only a single measurement was considered due to the strong deviation. All potentials were 100% iR-corrected.

2.6. X-ray Photoelectron Spectroscopy (XPS) and Scanning Electron Microscopy (SEM)

XPS measurements were conducted using a Thermo Scientific spectrometer, equipped with a monochromatic Al Kα X-ray source (1486.6 eV with a spot size of 400 nm). High-resolution spectra were acquired with 20 and 0.05 eV as the pass energy and step width, respectively. The XPS spectra were fitted using CasaXPS software, employing Gaussian−Lorentzian mixed peaks and a Shirley background. An asymmetric peak was applied exclusively to the C=C component. Calibration was done with respect to the C−C/C=C species at 284.8 eV. The binding energies of the fitted peaks are O 1s (lattice O) = 529.8 ± 0.1 eV, O 1s (O=C, Mn−OH) = 531.8 ± 0.1 eV, O 1s (O−C, ads. H_2O) = 533.2 ± 0.2 eV, Mn 3s (1) = 84.2 ± 0.2 eV, Mn 3s (2) = 89.5 ± 0.2 eV.

SEM images were taken from a field-emission-gun SEM (FEG-SEM, Zeiss Gemini 460 microscope) at low accelerating voltage (10 kV) in the secondary electron and backscattered electron mode, with a resolution of 0.7 nm.

2.7. Rotating Ring-Disk Electrode (RRDE)

RRDE experiments were performed in oxygen-saturated 0.1 M KOH (Emplura®, Merck). A glassy carbon disk electrode coated with the catalyst, a platinum ring electrode, an RHE (mini-Hydroflex, Gaskatel), and a platinum plate counter electrode were connected to the potentiostat (SP-300, Biologic). The ink used for drop-casting consisted of 20% α-MnO_2/C, 5 wt % Nafion D-520 dispersion (Ion Power), and a 1:1 water-isopropanol solution. The α-MnO_2 loading was ca. 40 μg cm^{-2}. Cyclic voltammograms between 0.0 and 1.0 V vs RHE were recorded at a scan rate of 10 mV s^{-1} while the ring electrode was held at 1.2 V vs RHE. The collection efficiency for the Pine E6-series RRDE is 0.256.

2.8. Synchrotron X-ray Diffraction (XRD)

XRD data were collected from the GDEs after AST at the ID31 beamline at the European Synchrotron Radiation Facility. A 2D Pilatus 2M CdTe detector was used at a distance of 1.55 m from the sample. The photon wavelength was 0.165 Å (75.00 keV). Raw diffraction patterns were radially integrated using PyFAI software package. Crystallite sizes were estimated using the Scherrer equation from selected α-MnO_2 reflections fitted with a Gaussian profile and linear background after subtracting instrumental broadening.

3. RESULTS AND DISCUSSION

To evaluate the catalyst capability for the ORR in alkaline media, assessing activity is not sufficient; durability must also be determined. An effective approach is IL-TEM, which enables

Downloaded from pubs.acs.org/acscatal/article-pdf/doi/10.1021/acscatal.6c06787/6916174/cs-2026-06787e.pdf by KIT BIBLIOTHEK user on 16 November 2026

https://doi.org/10.1021/acscatal.6c06787
ACS Catal. XXXX, XXX, XXX−XXX

morphological and structural changes to be established before and after an electrochemical experiment, consisting in this study of AST cycles with alternating three-second potential steps at 0.9 and 0.6 V vs RHE, simulating load cycling conditions. Similarly, three different measurement settings were selected to study the durability of 20% α-MnO_2/C: 0.1 M KOH at 25 °C, corresponding to standard lab conditions; 4.0 M KOH at 50 °C, representative for technical applications such as metal-air batteries;[14,28] and 4.0 M KOH at 25 °C, enabling better comparison between the two conditions. The corresponding IL-TEM images are shown in Figure 1, with a−c displaying overviews and d−f the corresponding detailed views before, after 1000 (1k), and after 5000 (5k) AST cycles.

Inspection of the images in Figure 1a−f reveals that cycling in 0.1 M KOH at 25 °C leads to clear changes. The roundish particles can be assigned to Vulcan and remain relatively stable. In contrast, the rod-shaped particle, identified as α-MnO_2, is strongly affected by the AST protocol. Noticeable dissolution is already observed after 1000 cycles and becomes even more pronounced after 5000 cycles. Significant portions of the particle disappear, and higher-magnification images show increased surface roughening. In addition, the nanorod thickness is reduced by approximately half. Interestingly, when the catalyst is exposed to the same electrolyte conditions but maintained at OCP, no significant changes are observed (Figure S3). This suggests that potential cycling, in particular, negatively affects the stability of α-MnO_2. Additional micrographs obtained using the same AST conditions as those shown in Figure 1a−f are displayed in Figures S4 and S5. Notably, Figure S5 does not exhibit the pronounced changes observed in the other examples. In this case, no Vulcan particles are present in the direct vicinity of the α-MnO_2. Since Vulcan is known to produce substantial amounts of peroxide species during the ORR,[29] it is plausible that locally formed peroxide contributes to the α-MnO_2 degradation and promotes its dissolution. Furthermore, the DEMS results shown in Figures S6d and S7d indicate that the presence of both α-MnO_2 and Vulcan significantly enhances the carbon oxidation reaction, which is most likely accompanied by reduction of α-MnO_2 and consequently leads to increased Mn dissolution. Additionally, carbon dioxide formed during carbon corrosion reacts in alkaline media with hydroxide to form carbonate species, thereby decreasing the local pH and further promoting α-MnO_2 dissolution.[16,30] These processes may also be responsible for the absence of pronounced α-MnO_2 degradation in the example discussed. For further details on the DEMS measurements, the reader is referred to the Supporting Information. In the case of 4.0 M KOH at 25 °C (Figures 1a′−f′ and S8), MnO_2 dissolution is more pronounced, and after 5000 AST cycles, only shadows of the α-MnO_2 particle remain visible. The degradation becomes even more severe at elevated temperatures. In 4.0 M KOH at 50 °C (Figure 1a″−f″), the α-MnO_2 nanorods have almost completely disappeared after 5000 AST cycles. Since MnO_2 is thermodynamically not stable at the applied potentials,[31] its surface gets reduced over time. So, the observations from the IL-TEM can be partially attributed to the increased solubility of the Mn^{II} and Mn^{III} species in higher alkaline molarities and at elevated temperatures.[32] In addition, Mn^{III} is particularly prone to disproportionation, which may further promote Mn dissolution by generating readily soluble Mn^{II} species.[33] These considerations may help explain the aforementioned absence of significant Mn dissolution in the absence of adjacent Vulcan since Mn reduction is not further accelerated. However, considering the low α-MnO_2 loading on the electrode (50 μg_{MnO_2} cm^{-2}) and the large excess of electrolyte used in this experiment, the changed solubility product alone is unlikely to be the main driving force. As all experiments were carried out using the same electrochemical protocol and at similar pH values, the thermodynamic conditions are comparable with respect to the Mn stability regions indicated in the Pourbaix diagram, and Mn^{IV} is thermodynamically unstable under these conditions.[31] Therefore, 40-fold higher KOH concentration and thus the substantially increased amount of hydroxide ions promote the Mn reduction and dissolution by facilitating Mn−O bond cleavage and subsequent Mn−OH formation at the particle surface. Additionally, elevated temperatures further accelerate both Mn reduction and dissolution kinetics, leading to more pronounced Mn dissolution. Thus, the comparison of these three conditions suggests that, while the thermodynamic instability of Mn^{IV} provides the driving force for its reduction, the differences in Mn dissolution are predominantly governed by kinetic effects.

In order to explain Mn dissolution after AST, the interplanar spacings calculated from the high-magnification IL-TEM images are summarized in Figure S9. Interplanar spacings of the pristine material confirm the presence of α-MnO_2 phase. Changes in interplanar spacing observed before and after AST can indicate phase transformations, structural modifications, or cation incorporation, which alter the Mn oxidation state and impact ORR performance and stability. Although minor variations are observed following AST, no statistically significant changes can be identified when considering the associated uncertainties and the fact that all pristine samples are expected to exhibit identical lattice parameters. Subtle changes in interplanar spacing may nevertheless occur but remain unresolved within the accuracy of the present analysis. In particular, K^+ incorporation into the tunnels of α-MnO_2 has been reported to induce lattice expansion and, consequently, increased interplanar spacing.[34,35] We postulate that such effects are not detectable in the present analysis, potentially because the gentle immersion in water after the electrochemical measurements removed a substantial fraction of the inserted K ions. Similarly, lattice expansion arising from elevated temperatures is reversible upon cooling[36] and is therefore not captured by the ex situ measurements performed here. Finally, amorphous regions could not be clearly identified by IL-TEM (see Figure S10). However, for the strongly dissolved regions and for the outermost layers of the MnO_2, the presence of a purely crystalline phase cannot be conclusively established.

To gain deeper insight into the mechanisms of the Mn dissolution, online ICP−MS measurements were performed in a flow cell setup. The electrochemical protocol consists of three cyclic voltammograms (CVs) between 0.9 and 0.6 V vs RHE, separated by an AST comprising 200 cycles of alternating three-second potential steps at 0.9 and 0.6 V vs RHE. While the corresponding current and potential profiles are shown in Figure 2a−d, Figure 2e,f display the time-resolved Mn dissolution rates obtained in a flow cell coupled to the ICP-MS using a 20% α-MnO_2/C catalytic layer. A first clear observation is that Mn dissolution is significantly more pronounced under oxygen than under argon atmosphere, as shown by the integrated Mn dissolution values (Figure 3a). During the AST, the total Mn dissolution under oxygen is about twice as high as that under argon. The dissolution profiles in Figure 2e,f further reveal distinct differences in their potential dependence. Under oxygen, a

Downloaded from pubs.acs.org/acscatsci/article-pdf/doi/10.1021/acscatal.6c06787/6916174/cs-2026-06787e.pdf by KIT BIBLIOTHEK user on 16 November 2026

https://doi.org/10.1021/acscatal.6c06787
ACS Catal. XXXX, XXX, XXX−XXX

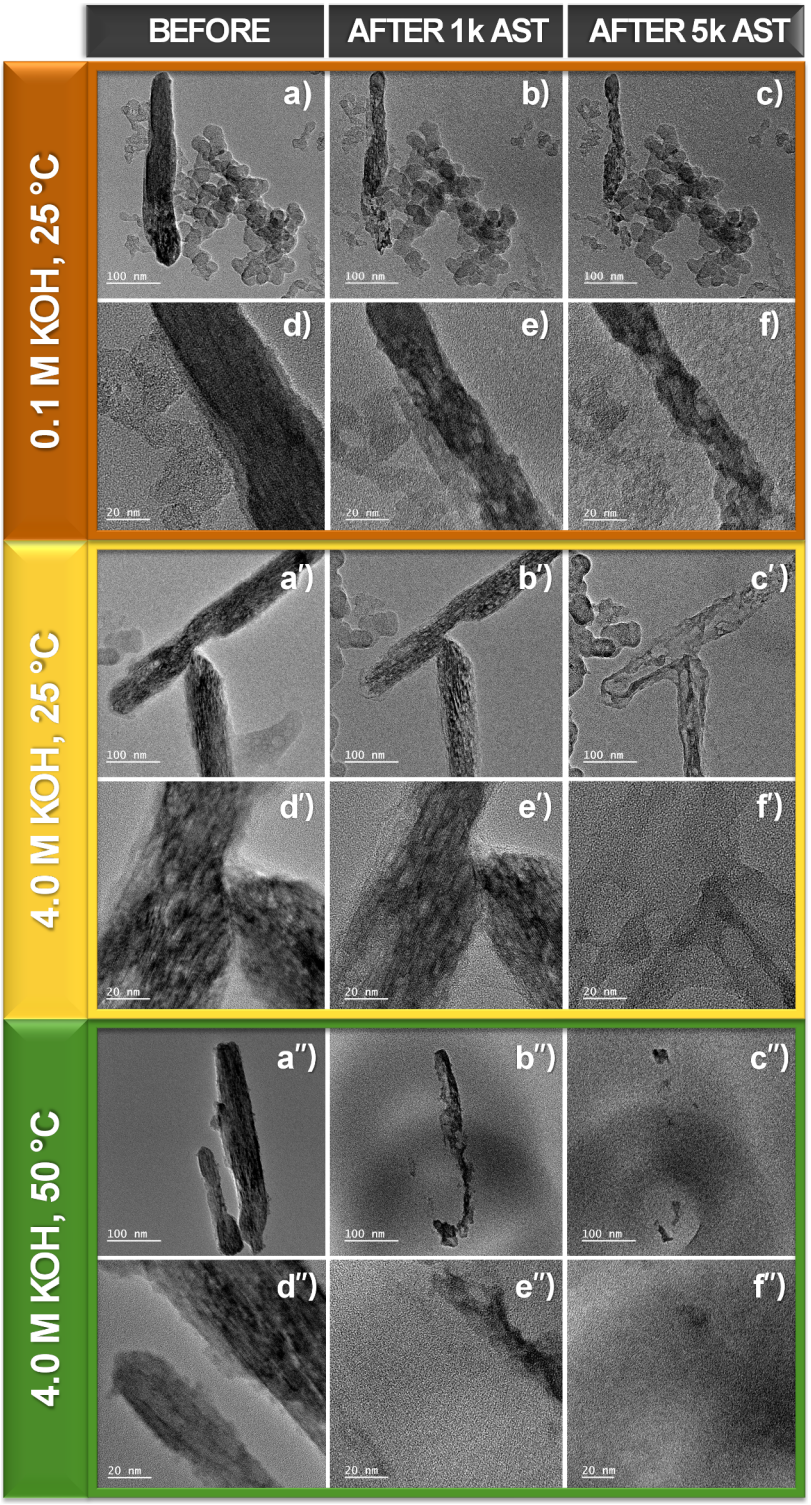


Figure 1. Identical location TEM images acquired before, after 1000 (1k), and after 5000 (5k) AST cycles, consisting of alternating 3 s steps at 0.6 and 0.9 V vs RHE. Electrochemical measurements were performed under three different conditions: 0.1 M KOH at 25 °C (a–f), 4.0 M KOH at 25 °C (a′–f′), and 4.0 M KOH at 50 °C (a″–f″).

single Mn dissolution maximum appears during the CV, located near the lower potential limit of 0.6 V vs RHE. In contrast, two Mn dissolution peaks are observed under argon: one near 0.6 V vs RHE during the negative sweep and a more pronounced peak at around 0.8 V vs RHE during the positive sweep. Similar observations under oxygen and argon conditions were reported by Speck et al.[18]

The enhanced Mn dissolution under oxygen can be attributed to the formation of peroxide species and other reactive oxygen species (ROS) during the ORR. ROS are generally less

Downloaded from pubs.acs.org/acscacs/article-pdf/doi/10.1021/acscatal.6c06787/6916174/cs-2026-06787e.pdf by KIT BIBLIOTHEK user on 16 November 2026

https://doi.org/10.1021/acscatal.6c06787
ACS Catal. XXXX, XXX, XXX–XXX

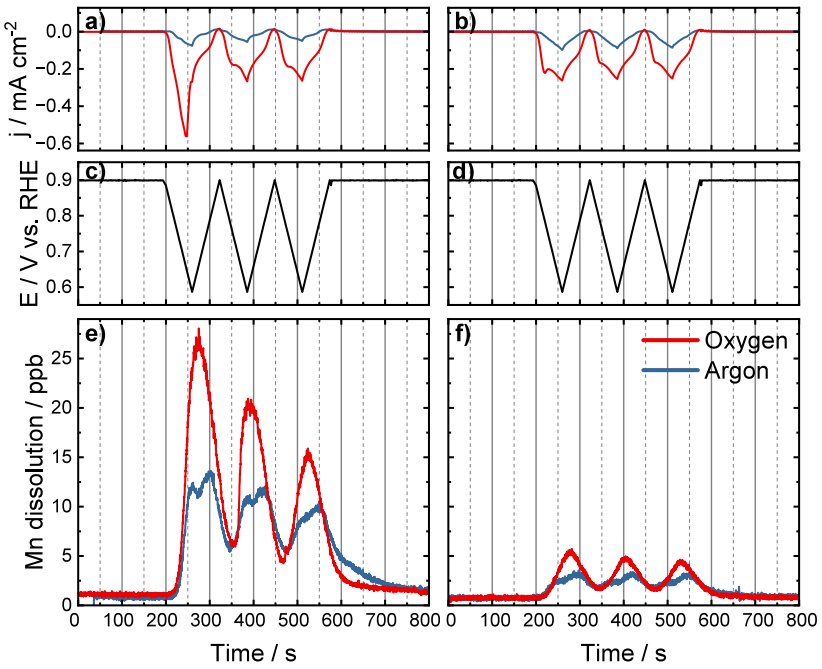


Figure 2. CVs with a scan rate of 5 mV s^{-1} with (a)/(b) current response and (c)/(d) applied potential profiles. (e)/(f) Comparison of the Mn dissolution measured in the flow cell setup coupled to the ICP-MS in argon- (blue) and oxygen-saturated (red) 0.1 M KOH. 200 AST cycles, consisting of alternating three-second potential steps at 0.9 and 0.6 V vs RHE, were performed between the profiles shown on the left and right. All potentials are iR-corrected.

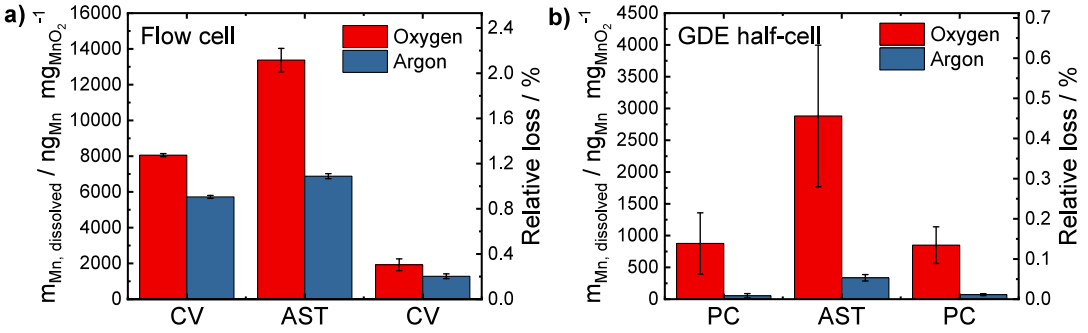


Figure 3. Mn dissolution according to the electrochemical program normalized by the MnO_2 loading (left axis) and by the relative Mn loss of the electrode (right axis) in (a) the flow cell and (b) the GDE half-cell coupled to the ICP-MS.

aggressive in alkaline than in acidic media due to the reduced formation of the highly reactive hydroxyl (•OH) radical. Instead, the ROS predominantly consist of the less reactive hydroperoxyl (•OOH) and hydrogen (•H) radical species.[37−39] Nevertheless, the RRDE results in Figure S11 reveal a peroxide yield of 5−16% in the potential range of 0−1 V vs RHE, with the peroxide yield increasing at higher overpotentials. Peroxides and related ROS can degrade MnO_2, thereby promoting its dissolution.[18] MnO_2 is known to efficiently decompose peroxide, particularly in alkaline media.[40] This reaction typically proceeds via Mn^{III} as the active site, which is oxidized to Mn^{IV} under alkaline conditions.[41] Mn^{III} is inherently present at the surface, as α-MnO_2 is non-stoichiometric and therefore contains a certain fraction of Mn^{III} species. Additionally, it is formed under ORR conditions upon reduction of MnO_2 and proton insertion,[9,17] which can also be observed in the CV in nitrogen-saturated electrolyte shown in Figure S12. The peak at 0.85 V vs RHE corresponds to that transition. Furthermore, XPS measurements have detected Mn^{III} after holding an α-MnO_2 electrode at 0.6 V vs RHE for 10 min, consistent with the thermodynamic preference for Mn^{III} under these conditions.[18,31] This observation is further supported by the XPS measurements presented in this study, which are discussed later. However, surface oxidation from Mn^{III} to Mn^{IV} during peroxide decomposition may induce surface restructuring, which facilitates transient Mn dissolution.[41] Transient dissolution during oxidation-state transitions is well documented for a variety of transition-metal oxides and has been attributed to structural and bonding rearrangements that can temporarily render the oxide more susceptible to dissolution in the metastable state, although the underlying mechanisms are not yet fully understood.[42] Moreover, the newly formed Mn^{IV} species are not thermodynamically favorable at the applied potentials, which may further contribute to Mn dissolution. In addition,

Downloaded from pubs.acs.org/acscacs/article-pdf/doi/10.1021/acscatal.6c06787/6916174/cs-2026-06787e.pdf by KIT BIBLIOTHEK user on 16 November 2026

https://doi.org/10.1021/acscatal.6c06787
ACS Catal. XXXX, XXX, XXX−XXX

Speck et al.[18] demonstrated that adding hydrogen peroxide to the electrolyte increases Mn dissolution independently of the applied potential, suggesting that peroxide, rather than the presence of oxygen or the ORR, cause the enhanced Mn dissolution.

Beyond ROS-induced degradation, the ORR mechanism itself also contributes to Mn dissolution. Indeed, it is widely accepted that the ORR on manganese dioxide proceeds via a mediated two-electron pathway involving the MnO_2/MnOOH redox couple, as supported by RRDE and in situ XANES studies, followed by peroxide disproportionation.[9,43−45] According to this mechanism, MnO_2 is first reduced to MnOOH (1), followed by the adsorption of O_2 (2). Subsequently, a slow charge-transfer step to the adsorbed O_2 occurs, during which MnOOH reacts back to MnO_2 (3), resulting in the formation of the peroxide species (4). The generated peroxide can then undergo a disproportionation reaction on the MnO_2 surface, producing molecular oxygen and hydroxide (5). If peroxide is fully disproportionated, the overall process effectively corresponds to a four-electron pathway. However, the repeated transition of the MnO_2/MnOOH redox couple may also lead to transient Mn dissolution.

$$Mn^{IV} + e^- \rightarrow Mn^{III} \quad (1)$$

$$O_2 \rightarrow O_{2,ads} \quad (2)$$

$$Mn^{III} + O_{2,ads} \rightarrow Mn^{IV} + O_{2,ads}^- \quad (3)$$

$$O_{2,ads}^- + H_2O + e^- \rightarrow HO_2^- + OH^- \quad (4)$$

$$2HO_2^- \rightarrow O_2 + 2OH^- \quad (5)$$

Reaction 5 may also proceed via two simultaneous steps.[43] In one pathway, peroxide is oxidized back to O_2 (6), whereas in the other, it is further reduced to hydroxide (7). This mechanism is consistent with our RRDE findings (Figure S11), which show increased peroxide formation at higher overpotentials. At these elevated overpotentials, the oxidation reaction (6), with a reversible potential of 0.695 V vs RHE,[46] becomes less thermodynamically favorable. Consequently, the reduction reaction (7), which depends on reaction (6), is also suppressed, thereby impeding the overall peroxide disproportionation.[46]

$$HO_2^- + OH^- \rightarrow O_2 + H_2O + 2e^- \quad 0.695\ V\ vs\ RHE \quad (6)$$

$$HO_2^- + H_2O + 2e^- \rightarrow 3OH^- \quad 1.776\ V\ vs\ RHE \quad (7)$$

Under argon, Mn dissolution mostly occurs through transient dissolution during redox transitions at the catalyst surface.[18] The potentials of the two Mn dissolution maxima observed under argon correspond well to the Mn_2O_3/Mn_3O_4 redox couple, which has a standard potential of 0.689 V vs RHE.[31] However, based on the mechanistic discussion above, MnOOH is more likely to be present than Mn_2O_3 and is expected to exhibit a similar redox potential.[43] Interestingly, we also noticed that the dissolution profile obtained under oxygen crosses that recorded under argon during the anodic scan. This suggests that, under oxygen, transient Mn dissolution during oxidation-state transitions does not proceed fully in parallel with ROS-induced degradation but is likely partially inhibited by the ongoing ORR. Finally, it is noteworthy that the Mn dissolution rate decreases within the first CVs when comparing successive cycles, as well as when comparing the CVs recorded after the AST. A similar behavior was reported by Rabe et al.,[47] who attributed this effect to the gradual formation of a passivation layer that suppresses further Mn dissolution over time.

Figure S13 displays a similar Mn dissolution experiment, focusing on the effect of varying the lower potential limit (LPL). The maximum of the Mn dissolution peak in oxygen-saturated electrolyte remains close to the LPL, exhibiting only a slight shift towards the anodic scan direction. Under argon, the Mn dissolution peak observed during the negative sweep disappears as the LPL is reduced. In contrast, the peak in the positive sweep remains but becomes noticeably broader. The broadening can be attributed to overlapping Mn dissolution processes, as the $Mn_3O_4/Mn(OH)_2$ redox couple occurs at 0.462 V vs RHE and thus lies within the cycled potential regime.[31] Moreover, $Mn(OH)_2$ readily dissolves in alkaline media,[32] which may further contribute to the observed signal broadening. The corresponding integrated Mn dissolution amounts are summarized in Figure S14a. Interpretation is complicated by the simultaneous decrease in dissolution rate over time, making it challenging to isolate the true contribution of the lower LPL. The first LPL measurement is identical to the preceding and final CVs. Therefore, the corresponding Mn dissolution data were fitted with an exponential decay function to approximate the Mn dissolution expected in the absence of LPL variation. This approach provides a rough estimate of the additional Mn dissolution arising from variation of the LPL. With this consideration, a lower LPL results in significantly increased Mn dissolution in oxygen-saturated electrolyte. This trend can be attributed to the larger exchanged charge, which promotes enhanced formation of ROS. Additionally, the peroxide formation yield also increases at lower potentials, as seen from the RRDE results (Figure S11). This observation is consistent with the previously described dissolution mechanism in oxygen-saturated electrolyte, in which peroxide and other ROS that do not directly disproportionate play a key role in the degradation of α-MnO_2 and promote Mn dissolution. Under argon, lowering the LPL leads only to a slight increase in Mn dissolution, which then remains nearly constant at more negative limits. Thus, decreasing the LPL has a substantially stronger impact on Mn dissolution in the presence of oxygen than with argon.

To quantify the dissolved Mn under operating conditions relevant to metal-air batteries or alkaline fuel cells, a modified GDE half-cell was coupled to the ICP-MS. Figure S15 presents a direct comparison between the flow cell and the GDE half-cell setup, both measured using identical electrochemical protocols in argon-saturated electrolyte. The small reduction current observed even under argon is likely attributable to residual oxygen in the setup, which is more pronounced in the GDE half-cell due to oxygen trapped within the GDL. Although the overall Mn dissolution profiles are similar for both setups, several distinct differences are evident. First, the anodic Mn dissolution peak appears at nearly the same potential in both configurations; however, the cathodic peak is almost absent in the GDE half-cell. Moreover, the pronounced anodic Mn dissolution peak in the GDE setup is accompanied by a significantly higher positive current response. These observations indicate

Downloaded from pubs.acs.org/acscatal/article-pdf/doi/10.1021/acscatal.6c06787/6916174/cs-2026-06787e.pdf by KIT BIBLIOTHEK user on 16 November 2026

https://doi.org/10.1021/acscatal.6c06787
ACS Catal. XXXX, XXX, XXX−XXX

that oxidation processes have a substantially stronger impact on Mn dissolution than reduction processes at the α-MnO_2 surface. Furthermore, an increasing *y*-offset appears over time in the GDE half-cell setup. This is attributed to differences in cell design. In the online flow cell, all electrolyte, along with all dissolved Mn species, is continuously transported to the ICP-MS. In contrast, in the GDE half-cell, dissolved Mn species accumulate in the electrolyte compartment, and only a fraction of it is pumped to the ICP-MS. To account for this difference, a collection efficiency is applied to the GDE half-cell measurements (please refer to the Supporting Information for details). Nevertheless, dissolved Mn species progressively accumulate in the electrolyte reservoir of the GDE half-cell, resulting in an increasing background signal over time. A direct comparison of the dissolution profiles (Figure S15e,f) reveals similar Mn dissolution trends. However, after normalizing for differences in α-MnO_2 loading and geometrical active surface area, the total Mn dissolution in the flow cell is about one order of magnitude greater than in the GDE half-cell (Figure S14b). This difference primarily arises from distinct flow conditions. In the flow cell, pronounced hydrodynamic forces facilitate the detachment of weakly bound Mn species from the thin catalyst film (10 μg_{MnO2} cm^{-2}). Furthermore, continuous electrolyte flow rapidly removes dissolved Mn species from the electrode vicinity, thereby shifting the dissolution equilibrium toward further Mn dissolution. By contrast, in the GDE half-cell, Mn species are only partially wetted by electrolyte under nearly static conditions, resulting in comparatively slower dissolution rates due to mass-transport limitations.

Importantly, Mn dissolution quantities can be directly compared in the GDE half-cell under oxygen and argon conditions. Due to the significant iR drop in the GDE half-cell configuration, current-controlled instead of potential-controlled measurements were performed under oxygen conditions. The electrochemical protocol follows previously reported procedures for the GDE half-cell coupled to the ICP-MS.[23,24] Stepwise increasing current densities were applied to construct a polarization curve (PC) and to match the potentials used in the argon measurements (Figure 4a,b). Current interruptions between the steps improve the separation of the ICP-MS signal. As shown in Figure 4c,d, the resulting potentials under oxygen and argon conditions are in good agreement, enabling a meaningful comparison of Mn dissolution behavior under both conditions (Figure 4e,f). Under argon, Mn dissolution can barely be detected starting from the second step at 0.794 V vs RHE and more significantly in the third step at 0.769 V vs RHE. Under oxygen, a Mn dissolution signal already appears during the first step. However, this signal is associated with the subsequent EIS measurements at slightly higher applied currents rather than the current step itself. In the following current steps, Mn dissolution becomes clearly visible. In both oxygen- and argon-saturated electrolytes, the intensity of the Mn dissolution peaks increases with decreasing potential, confirming the results obtained from LPL measurements in the flow cell. Furthermore, the background signal increases substantially under oxygen conditions, particularly when comparing data acquired before and after AST.

Compared to the flow cell measurements, the Mn dissolution signals measured in the GDE half-cell under oxygen are broader, and in some cases, Mn dissolution peaks appear even when no current is applied. This behavior might be explained by particles that get loosened during the applied current step but dissolve with a delay after the step has ended. The integrated Mn dissolution amounts in Figure 3b are approximately 10 times higher under oxygen than under argon. We attribute this to the 50-fold higher currents applied in the GDE half-cell,

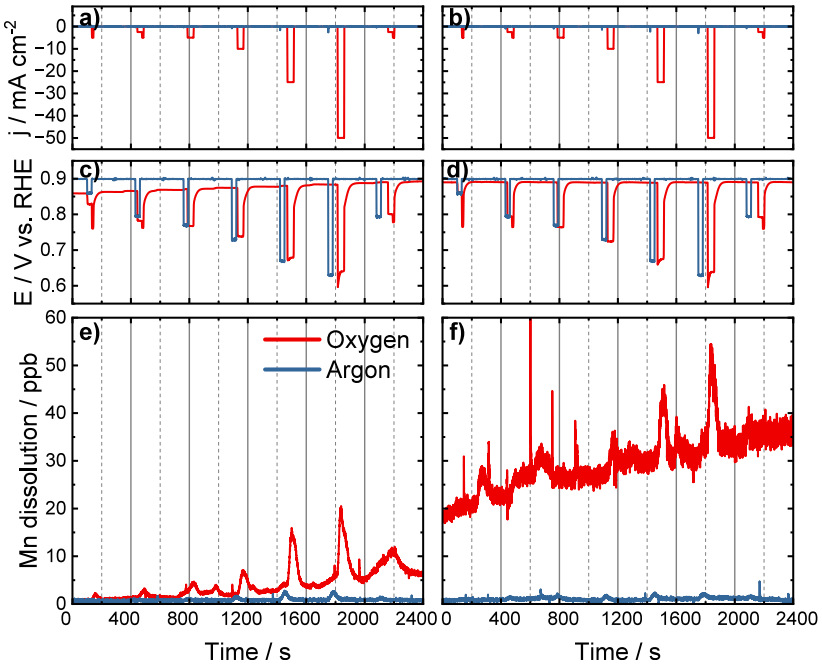


Figure 4. (a)/(b) Current and (c)/(d) corresponding potential profiles. (e)/(f) Comparison of the Mn dissolution measured in the GDE half-cell coupled to the ICP-MS in argon- (blue) and oxygen-saturated (red) 0.1 M KOH. Between the profiles shown on the left and right, 200 AST cycles were performed, consisting of alternating three-second potential steps at 0.9 and 0.6 V vs RHE under argon and applied current steps at −0.01 mA cm^{-2} and −50 mA cm^{-2} under oxygen. All potentials are iR-corrected.

https://doi.org/10.1021/acscatal.6c06787
ACS Catal. XXXX, XXX, XXX−XXX

Downloaded from pubs.acs.org/acscatal/article-pdf/doi/10.1021/acscatal.6c06787/6916174/cs-2026-06787e.pdf by KIT BIBLIOTHEK user on 16 November 2026

which promote the formation of larger amounts of ROS and thereby enhance Mn dissolution. Additionally, the error bars for the GDE half-cell under oxygen are larger, indicating lower reproducibility than in the flow cell experiments. This reflects the intrinsic differences between the two configurations. Whereas the smooth glassy carbon disk electrode is fully and uniformly exposed to oxygen-saturated electrolyte, similar to the situation in a fuel cell cathode, the GDE exhibits a much broader range of local catalyst microenvironments arising from variations in gas and liquid phase distribution. In summary, the Mn dissolution profiles in the flow cell are clearer and more distinct, facilitating the determination of the Mn dissolution mechanism, while the GDE half-cell measurement yields more realistic Mn dissolution amounts under technically relevant conditions.

Additionally, the S-number is introduced as a measure of catalyst stability and is defined here as the number of electrons transferred per dissolved Mn atom. Figure S16 displays the S-number as a function of potential and current density for the experiment shown in Figure 4. All values are within the same order of magnitude, around 10^5, and remain relatively stable across the applied potentials and current densities. This behavior suggests that Mn dissolution under oxygen is predominantly governed by ROS-induced degradation. However, the lowest potential value exhibits an increase in the S-number, which may be attributed to an outlier, as indicated by the large error bar. Nevertheless, a slight increase in the S-number with increasing current density and decreasing potential is also apparent across the entire range. This trend may be explained by a reduced dissolution rate over time, as also observed in the flow cell, since the higher potentials and lower current densities were measured first. Alternatively, it may result from simultaneous transient dissolution associated with Mn oxidation state transition, which becomes relatively less pronounced at higher current densities.

IL-TEM images and ICP-MS data reveal pronounced morphological changes and provide insights into the underlying dissolution mechanisms, respectively. To evaluate the influence of these changes on ORR performance, GDE half-cell measurements were performed over a total of 5000 AST cycles. To ensure comparability across the wide range of conditions, current densities were selected to target a lower potential limit of 0.6 V vs RHE and an upper potential limit close to the OCP. This protocol required a relatively low α-MnO_2 loading of 50 μg cm^{-2}, which limits the achievable ORR performance. The full performance of 20% α-MnO_2/C electrodes is discussed in our previous publication.[14] Figure 5a–c presents the polarization curves obtained under identical conditions as used for the IL-TEM measurements. In 0.1 M KOH at 25 °C, a continuous decrease in ORR performance is observed after each set of AST cycles (Figure 5a), which may be attributed to a reduction in the electrochemically active surface area (ECSA). Unfortunately, no established method exists to determine the ECSA of MnO_2, as is the case for Pt catalysts. However, changes in ECSA can be inferred based on the IL-TEM and ICP-MS results.

A completely different trend is observed in 4.0 M KOH at 25 °C (Figure 5b). Starting from the first polarization curve, an improvement in ORR performance is evident. This unexpected behavior can be attributed either to an increased ECSA, consistent with the surface roughening seen in the IL-TEM micrographs (Figure 1a′–f′), resulting from the activation and functionalization of Vulcan XC72R in highly alkaline molarities,[48] which partly explains the enhanced ORR activity, or the formation of more active Mn surface species. In the literature, it is widely accepted that an optimal Mn^{III}/Mn^{IV} ratio, often associated with oxygen vacancies, enhances the overall ORR activity of α-MnO_2. This improvement is attributed to the presence of a single unpaired electron on the e_g orbital of Mn^{III}, which promotes optimal adsorption of *OOH, *O, and *OH intermediates in accordance with the reaction sequence (1) − (5) described above.[8,49] After 5000 AST cycles, however, the ORR performance returns to approximately its initial level, indicating increased Mn dissolution, consistent with the IL-TEM observations. In 4.0 M KOH at 50 °C, a similar initial trend is observed. However, after only 500 AST cycles, the ORR performance starts to decline and falls below the initial

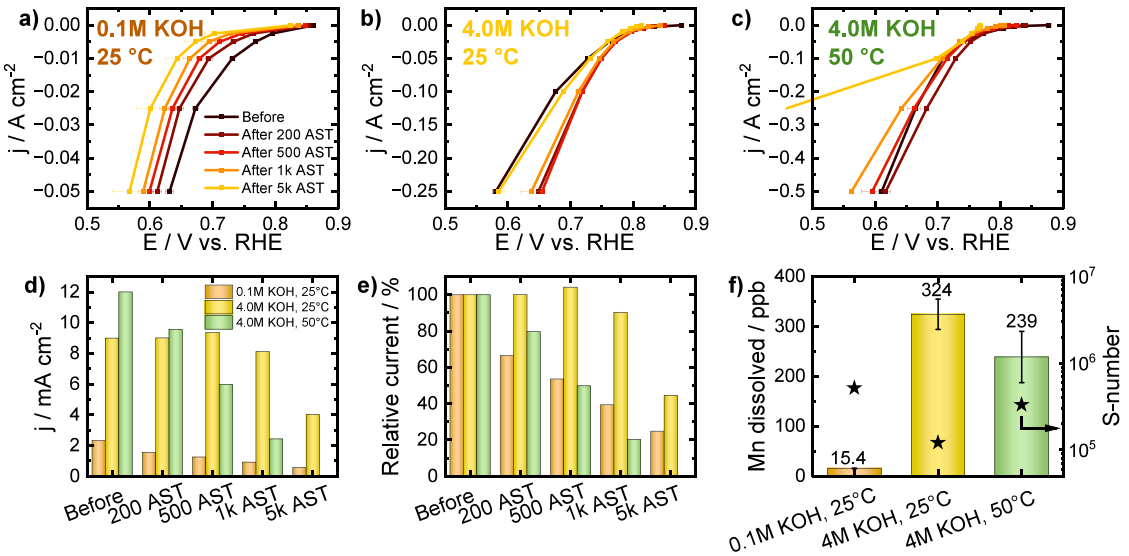


Figure 5. Polarization curves measured before and after ASTs in (a) 0.1 M KOH at 25 °C, (b) 4.0 M KOH at 25 °C, and (c) 4.0 M KOH at 50 °C. (d) Current density at 0.8 V vs RHE for different measurement conditions, and (e) the corresponding relative current at 0.8 V vs RHE. (f) Concentration of dissolved Mn in the electrolyte after the complete 5k AST protocol under the respective conditions (left axis) and corresponding S-number (right axis).

https://doi.org/10.1021/acscatal.6c06787
ACS Catal. XXXX, XXX, XXX–XXX

Downloaded from pubs.acs.org/acscatal/article-pdf/doi/10.1021/acscatal.6c06787/6916174/cs-2026-06787e.pdf by KIT BIBLIOTHEK user on 16 November 2026

level. After 5000 cycles, a pronounced decrease in ORR performance is visible, which can be attributed to electrode flooding caused by surface functionalization of Vulcan, as discussed in detail in the Supporting Information (*cf.* Figure S17 and accompanying text).

Figure 5d,e present the current densities at 0.8 V vs RHE under the different conditions in absolute and relative terms, respectively. The 4.0 M KOH at 50 °C shows the best initial ORR performance. The increased KOH concentration enhances ORR kinetics, which can be attributed to the stabilization of ORR intermediates, such as superoxide ($\cdot O_2^-$), and a consequent lowering of the energy barriers of individual ORR reaction steps, leading to an increased exchange current density.[50,51] KOH concentrations in the range of 2−4 M have been reported to yield the best ORR performance for MnO_2 catalysts.[45] Additionally, ionic conductivity increases at elevated temperatures, enhancing mass transport.[52] However, this trend reverts after 500 AST cycles. Both in absolute and relative numbers, the experiment with 4.0 M KOH at 25 °C surpasses the others in ORR performance and even shows a slight improvement to the initial level, likely due to surface roughening of the catalyst. In contrast, a steady decline in ORR performance is observed with 4.0 M KOH at 50°C, attributed to severe Mn dissolution, as also indicated by IL-TEM micrographs (Figure 1). The higher applied currents and the associated increased formation of peroxide species further promote this effect. Interestingly, from 500 AST cycles onward, the 4.0 M KOH at 25 °C condition maintains the highest ORR performance for the rest of the experiment. This trend is unexpected when considering the Mn concentrations in the electrolyte after the end of the experiment (Figure 5f). The lowest Mn concentration is detected for 0.1 M KOH at 25 °C, approximately 21 times lower than that measured in 4.0 M KOH at 25 °C. This is surprising as the relative current decay is more pronounced in 0.1 M KOH at 25 °C (Figure 5e). The higher relative current retained in 4.0 M KOH at 25 °C, despite significantly more Mn dissolution, must therefore be explained either by a largely preserved ECSA or by the formation of more active Mn surface species, as discussed above. Additionally, part of the better performance can be attributed to the functionalization of Vulcan XC72R, which is a gradual process under ORR conditions, particularly in highly alkaline molarities. The values obtained for 4.0 M KOH at 50 °C are difficult to interpret quantitatively due to electrode flooding, which also accounts for the comparatively large error bars. Nevertheless, it is reasonable to assume that in the absence of flooding, even higher Mn concentrations would have been detected. To account for the different applied current densities, the S-number is additionally introduced on the right axis of Figure 5f. For the first two conditions, the S-numbers are 518,000 and 122,000, respectively. These values are approximately one order of magnitude lower than the value reported for a commercial Fe−N−C catalyst, which was approximately 10^6.[23] Interestingly, the substantially smaller variation in the S-numbers compared with the dissolved Mn concentrations under the different conditions indicates that the amount of charge passed is a key factor governing Mn dissolution. This can be rationalized by the fact that a fraction of the transferred charge contributes to peroxide formation, which in turn promotes Mn dissolution. The remaining difference between the S-numbers suggests that the rate of peroxide formation may also be affected by increasing KOH concentration and temperature. However, additional factors such as the higher solubility of Mn^{II} and Mn^{III} species[32] as well as the generally accelerated reaction and dissolution kinetics in concentrated KOH also contribute to the enhanced Mn dissolution and the decreased S-number observed at higher KOH concentrations, consistent with the IL-TEM observations (Figure 1).

Figure 6 presents the XPS spectra of the pure α-MnO_2 catalyst, the pristine GDE, the GDE after 5000 AST cycles in 0.1 M KOH at 25 °C, and after 5000 AST cycles in 4.0 M KOH at 25 °C (from top to bottom). The electrode subjected to 5000 AST cycles in 4.0 M KOH at 50 °C is not included, as no Mn signal was detected. Together with the pronounced electrode flooding, the complete loss of the Mn signal explains the poor ORR performance in the last polarization curve (Figure 5c). Significant spectral changes are already observed when comparing the pure α-MnO_2 catalyst with the pristine electrode. The Mn 3s peak splitting increases from 4.66 to 5.33 eV. The Mn 3s peak splitting energy (ΔE) is commonly

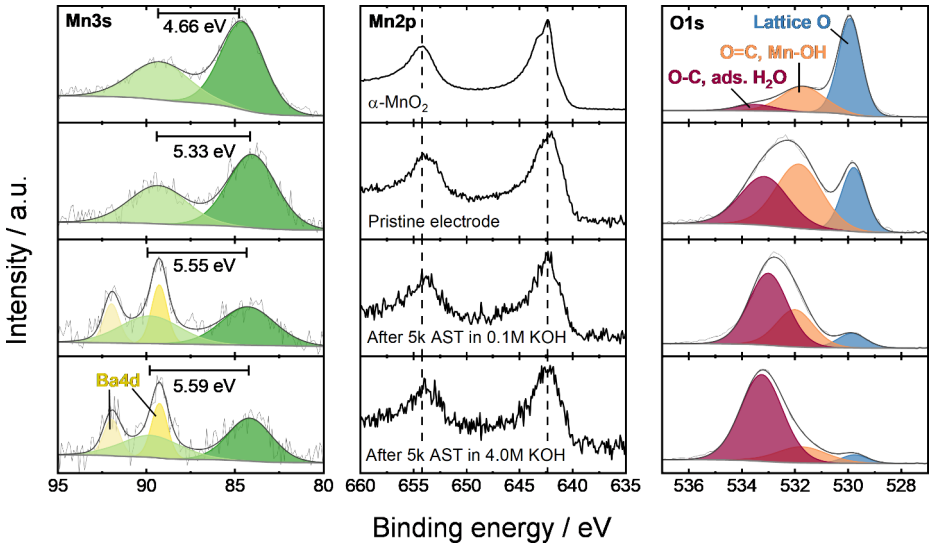


Figure 6. XPS spectra of α-MnO_2 powder and pristine 20% α-MnO_2/C loaded GDE, after 5000 AST cycles in 0.1 M KOH at 25 °C, and after 5000 AST cycles in 4.0 M KOH at 25 °C, from top to bottom, respectively. The Mn 3s spectra include the corresponding peak-splitting energies.

https://doi.org/10.1021/acscatal.6c06787
ACS Catal. XXXX, XXX, XXX−XXX

Downloaded from pubs.acs.org/acscatal/article-pdf/doi/10.1021/acscatal.6c06787/6916174/cs-2026-06787e.pdf by KIT BIBLIOTHEK user on 16 November 2026

used to estimate the average oxidation state (AOS) according to: AOS = 8.956 − 1.126 ΔE.[53] Using this relation, AOS values of 3.7 (pure catalyst) and 3.0 (pristine electrode) are obtained. The peak splitting energy of the pure catalyst is consistent with reported values for α-MnO_2.[54,55] The deviation to the formal oxidation state of 4.0 reflects the non-stoichiometric nature of α-MnO_2, which possesses the most open crystal structure among the MnO_2 polymorphs.[56] The AOS of the pristine electrode indicates that the surface is predominantly composed of Mn^{III} species. This is unexpected, as such a reduction in oxidation state was anticipated only after prolonged immersion and electrochemical cycling in alkaline electrolyte. Instead, the electrode fabrication process already induces the formation of Mn^{III} surface species. This finding is further supported by the slight shift of the Mn 2p peaks towards lower binding energies and by changes in the O 1s region, where a decrease in lattice oxygen is accompanied by an increase in Mn−OH species. After the electrochemical AST experiments, the Mn 3s peak splitting energy further increases to approximately 5.6 eV, corresponding to an AOS of about 2.7. The Ba 4d peak doublet is also detected at an atomic percentage more than 50-fold lower than that of Mn, likely arising from trace impurities in the KOH electrolyte. No clear difference in AOS is observed between the two electrolyte concentrations. The further decrease in AOS suggests progressive surface reduction, consistent with the thermodynamic preference for Mn^{III} under the applied potentials.[31] This behavior is further supported by the RDE results shown in Figure S18. When cycling 20% α-MnO_2/C between 0 V and 1 V vs RHE in 0.1 M KOH, the first cycle displays a pronounced reduction peak at around 0.5 V vs RHE. In the following cycles, the ORR activity decreases markedly, which can be attributed to changes in the catalyst oxidation state and possible Mn dissolution. Therefore, maintaining a narrower potential window, e.g., by increasing the LPL to about 0.7 V vs RHE, could help preserve the ORR activity for a longer time. As discussed previously, ORR activity depends on an optimal Mn^{III}/Mn^{IV} ratio. While Mn^{III} surface species are considered beneficial active sites, a fully Mn^{III} compound, such as Mn_2O_3, typically exhibits lower ORR activity, likely due to its different crystal structure and lack of the open tunnel framework.[10,49] In contrast, α-MnO_2 provides a (2 × 2) crystal tunnel structure that facilitates ion diffusion and transport. Ideally, high ORR performance is achieved when Mn^{III} surface species are present while the α-MnO_2 structural backbone remains intact. However, distinguishing such surface-bulk relationships is challenging with XPS due to its inherent surface sensitivity.

The similar XPS results obtained for the two different KOH concentrations suggest that the enhanced ORR performance observed after the first few hundred AST cycles in 4.0 M KOH at 25 °C does not arise from an increased fraction of Mn^{III} species. Instead, the improvement is more likely attributable to an increased ECSA, primarily resulting from surface roughening and, to a lesser extent, from the partial activation of the Vulcan support. The less direct correlation between the GDE half-cell results and the IL-TEM observations can be explained by differences in the setups. In the IL-TEM experiments, similar to the flow cell ICP-MS measurements, the catalyst is fully immersed in a large excess of electrolyte. In contrast, in the GDE half-cell, the inner MnO_2 particles are only exposed to the electrolyte via pores. Consequently, the IL-TEM conditions can be considered more aggressive and facilitate Mn dissolution compared to those in the GDE half-cell. This interpretation is further supported by the Mn concentrations measured after the GDE experiments (Figure 5f), which are lower than would be expected based on the IL-TEM observations.

Furthermore, SEM micrographs of the GDEs recorded after the electrochemical measurements still reveal the presence of α-MnO_2 particles (Figure S19). Consistently, the particle size distributions derived from *post mortem* TEM images (Figure S20) indicate largely stable particle dimensions under most conditions. The only notable exception is with 4.0 M KOH at 50 °C, where substantially smaller particle sizes and partially hollow particle morphologies are observed. Using Rietveld refinement, we found the crystallite sizes determined by XRD are consistently smaller than the particle sizes obtained from TEM analysis (Figure S21). This discrepancy likely arises because individual particles are composed of multiple crystallites. In addition, the average particle size determined from TEM may be biased toward larger particles, as smaller particles are harder to identify and are consequently underrepresented in the analysis.

In conclusion, these results indicate that the catalyst undergoes structural changes during the AST, evolving from a pure α-MnO_2 to a surface consisting of a Mn^{III} species, most likely MnOOH, while retaining an α-MnO_2 backbone that progressively decreases in size during the AST. Additionally, these observations highlight the importance of evaluating catalyst degradation not only under standard lab but also under technically relevant conditions, as degradation mechanisms and rates may differ substantially between the two.

4. CONCLUSION

The durability of α-MnO_2 during the ORR was examined under both standard lab conditions (0.1 M KOH, 25 °C) and under more technically relevant conditions (4.0 M KOH, 50 °C). An intermediate condition (4.0 M KOH, 25 °C) was included to decouple the effects of electrolyte concentration and temperature. Mechanistic and application-relevant insights into α-MnO_2 catalyst degradation were obtained using a combination of characterization techniques, including IL-TEM, RRDE, DEMS, online ICP-MS coupled to both flow cell and GDE half-cell, as well as GDE half-cell measurements followed by *post mortem* XPS, XRD, TEM, and SEM analyses.

IL-TEM imaging reveals pronounced morphological changes of α-MnO_2 during electrochemical cycling, whereas the carbon support (Vulcan) remains stable. Higher KOH concentrations and elevated temperatures significantly increase Mn dissolution, mainly reflecting accelerated Mn reduction and dissolution kinetics. Online ICP-MS measurements demonstrate that Mn dissolution is substantially higher under oxygen than under argon, highlighting the important role of ORR-derived ROS. This ROS-induced degradation becomes more pronounced at higher overpotentials, and RRDE measurements correlate this behavior with increasing peroxide formation. These observations are consistent with previously proposed ORR mechanisms on manganese dioxide, in which the reaction proceeds via a mediated two-electron pathway involving the MnO_2/MnOOH redox couple.

The complementary use of two ICP-MS-coupled electrochemical setups further highlights their respective strengths. The online flow cell provides high temporal and potential resolution of dissolution events, thereby facilitating mechanistic interpretation, whereas the GDE half-cell allows quantification of Mn dissolution under conditions that are closer to practical device operation.

Downloaded from pubs.acs.org/acscatal/article-pdf/doi/10.1021/acscatal.6c06787/6916174/cs-2026-06787e.pdf by KIT BIBLIOTHEK user on 16 November 2026

https://doi.org/10.1021/acscatal.6c06787
ACS Catal. XXXX, XXX, XXX−XXX

Despite the substantially increased Mn dissolution at higher electrolyte concentrations, the GDE measurements reveal a significantly improved initial ORR performance in concentrated KOH (4.0 M KOH, 25−50 °C). This enhancement is attributed to the stabilization of ORR intermediates and increased ionic conductivity in highly alkaline electrolyte. Notably, after 5000 AST cycles, the highest ORR performance is observed for 4.0 M KOH at 25 °C, despite the Mn concentration in the electrolyte being approximately 21-fold higher than under standard lab conditions (0.1 M KOH, 25 °C). As the Mn oxidation state after the experiment is comparable for both conditions (average Mn oxidation state = 2.7), the improved performance is unlikely to originate from changes in Mn speciation. Instead, it is most plausibly associated with an increased electrochemically active surface area resulting from surface roughening. Partial contribution arising from the functionalization of the carbon Vulcan support cannot be excluded. The performance of the α-MnO_2 catalyst in 4.0 M KOH at 50 °C could not be fully assessed due to electrode flooding, which may be mitigated in future studies by optimizing the gas diffusion layer.

Overall, the results highlight the importance of studying catalyst degradation under application-relevant operating conditions, as degradation mechanism and performance evolution can differ significantly from those observed under standard laboratory conditions.

The experimental findings suggest three dominant degradation pathways:

- Under oxygen-free conditions, Mn dissolution is primarily driven by transient dissolution associated with changes in Mn oxidation state;
- Under oxygen conditions, peroxide and other ROS generated during the ORR additionally promote Mn dissolution, resulting in significantly higher degradation rates;
- At low electrode potentials, Mn dissolution is further enhanced, consistent with increased peroxide formation at higher ORR overpotentials, and the reduction of Mn^{IV} to Mn^{III} and Mn^{II} species, which are substantially more soluble than Mn^{IV}.[32]

These findings indicate that the use of α-MnO_2 as an ORR catalyst is best suited to short-duration applications, such as primary metal-air batteries. For extended operation, additional strategies are required to mitigate catalyst degradation. These may include restricting the operating potential window (e.g., avoiding potentials below 0.7 V vs RHE) and applying protective catalyst coatings to suppress Mn dissolution. When using application-relevant catalyst loadings, solubility constraints may partially limit Mn dissolution. Finally, although higher KOH concentrations accelerate Mn dissolution, they also enhance the ORR activity and can deliver superior long-term performance. Taken together, these results underscore the complex interplay between catalytic activity and durability, and highlight that higher activity does not necessarily come at the expense of catalyst lifetime.

■ ASSOCIATED CONTENT

Supporting Information

The Supporting Information is available free of charge at https://pubs.acs.org/doi/10.1021/acscatal.6c06787.

Additional experimental details, characterizations, and electrochemical measurements (DOCX)

■ AUTHOR INFORMATION

Corresponding Authors

Alexander Rampf − *Univ. Grenoble Alpes, Univ. Savoie Mont Blanc, CNRS, Grenoble INP (Institute of Engineering and Management, Univ. Grenoble Alpes), LEPMI, Grenoble 38000, France; Karlsruhe Institute of Technology, Helmholtz Institute Ulm, Helmholtzstraße 11, Ulm 89081, Germany; Friedrich-Alexander-Universität Erlangen-Nürnberg, Chair of Electrochemical and Electrical Energy Technologies, Cauerstraße 9, Erlangen 91058, Germany;* orcid.org/0009-0000-1300-5431; Email: alexander.rampf@kit.edu

Kavita Kumar − *Univ. Grenoble Alpes, Univ. Savoie Mont Blanc, CNRS, Grenoble INP (Institute of Engineering and Management, Univ. Grenoble Alpes), LEPMI, Grenoble 38000, France;* orcid.org/0000-0003-3844-1082; Email: kavita.kumar@grenoble-inp.fr

Authors

Vincent Martin − *Univ. Grenoble Alpes, Univ. Savoie Mont Blanc, CNRS, Grenoble INP (Institute of Engineering and Management, Univ. Grenoble Alpes), LEPMI, Grenoble 38000, France;* orcid.org/0000-0002-9521-4137

Michal Ronovský − *Univ. Grenoble Alpes, Univ. Savoie Mont Blanc, CNRS, Grenoble INP (Institute of Engineering and Management, Univ. Grenoble Alpes), LEPMI, Grenoble 38000, France;* orcid.org/0000-0002-8702-6056

Andres O. Godoy − *Forschungszentrum Jülich GmbH, Helmholtz Institute Erlangen-Nürnberg for Renewable Energy (HI ERN), Cauerstraße 1, Erlangen 91058, Germany;* orcid.org/0000-0002-6858-2962

Thomas Diemant − *Karlsruhe Institute of Technology, Helmholtz Institute Ulm, Helmholtzstraße 11, Ulm 89081, Germany;* orcid.org/0000-0001-9701-9995

Frédéric Maillard − *Univ. Grenoble Alpes, Univ. Savoie Mont Blanc, CNRS, Grenoble INP (Institute of Engineering and Management, Univ. Grenoble Alpes), LEPMI, Grenoble 38000, France;* orcid.org/0000-0002-6470-8900

Marian Chatenet − *Univ. Grenoble Alpes, Univ. Savoie Mont Blanc, CNRS, Grenoble INP (Institute of Engineering and Management, Univ. Grenoble Alpes), LEPMI, Grenoble 38000, France;* orcid.org/0000-0002-9673-4775

Roswitha Zeis − *Karlsruhe Institute of Technology, Helmholtz Institute Ulm, Helmholtzstraße 11, Ulm 89081, Germany; Friedrich-Alexander-Universität Erlangen-Nürnberg, Chair of Electrochemical and Electrical Energy Technologies, Cauerstraße 9, Erlangen 91058, Germany; University of Toronto, Department of Mechanical and Industrial Engineering, 5 King's College Road, Toronto, Ontario M5S 3G8, Canada;* orcid.org/0000-0001-8379-0578

Complete contact information is available at: https://pubs.acs.org/doi/10.1021/acscatal.6c06787

Author Contributions

A.R.: Conceptualization, data curation, formal analysis, investigation, methodology, and writing—original draft; V.M.: Investigation, data curation, formal analysis, and writing—review & editing; M.R.: Investigation, data curation, formal analysis, and writing—review & editing; A.G.: Formal analysis and writing—review & editing; T.D.: Formal analysis and

Downloaded from pubs.acs.org/acscatal/article-pdf/doi/10.1021/acscatal.6c06787/6916174/cs-2026-06787e.pdf by KIT BIBLIOTHEK user on 16 November 2026

https://doi.org/10.1021/acscatal.6c06787
ACS Catal. XXXX, XXX, XXX−XXX

writing—review & editing; F.M.: Conceptualization, investigation, funding acquisition, and writing—review & editing; K.K.: Conceptualization, investigation, supervision, and writing—review & editing; M.C.: Conceptualization, investigation, supervision, funding acquisition, and writing—review & editing; R.Z.: Conceptualization, supervision, funding acquisition, and writing—review & editing.

Notes

The authors declare no competing financial interests.

■ ACKNOWLEDGMENT

Alexander Rampf received the KHYS Research Travel Grant from the Karlsruhe House of Young Scientists (KHYS) for financial support during his research stay in Grenoble. We thank Thomas Gaumont for determining the spray-coating machine parameters and calculating the ink composition. We thank Camille Jourdin for conducting the spray-coating of the GDEs. Some of this work has been made using characterization equipment funded by the Centre of Excellence of Multifunctional Architectured Materials "CEMAM" (grant number ANR-10-LABX-44-01). This work is part of the ALU-STORE project (Aluminum Metal as Energy Carrier for Seasonal Energy Storage) funded by the KIT Future Fields. This work contributes to the research performed at CELEST (Center for Electrochemical Energy Storage Ulm-Karlsruhe).

■ REFERENCES

(1) Kwon, N. H.; Lee, K. G.; Kim, H. K.; Hwang, S. J. MnO_2-Based Nanostructured Materials for Various Energy Applications. *Mater. Chem. Front.* **2021**, *5* (9), 3549−3575.

(2) Tang, Y.; Zheng, S.; Xu, Y.; Xiao, X.; Xue, H.; Pang, H. Advanced Batteries Based on Manganese Dioxide and Its Composites. *Energy Storage Mater.* **2018**, *12*, 284−309.

(3) Li, Y.; Dai, H. Recent Advances in Zinc-Air Batteries. *Chem. Soc. Rev.* **2014**, *43* (15), 5257−5275.

(4) Stoerzinger, K. A.; Risch, M.; Han, B.; Shao-Horn, Y. Recent Insights into Manganese Oxides in Catalyzing Oxygen Reduction Kinetics. *ACS Catal.* **2015**, *5* (10), 6021−6031.

(5) Yin, M.; Miao, H.; Hu, R.; Sun, Z.; Li, H. Manganese Dioxides for Oxygen Electrocatalysis in Energy Conversion and Storage Systems over Full PH Range. *J. Power Sources* **2021**, *494*, 229779.

(6) Cheng, F.; Su, Y.; Liang, J.; Tao, Z.; Chen, J. MnO_2-Based Nanostructures as Catalysts for Electrochemical Oxygen Reduction in Alkaline Media. *Chem. Mater.* **2010**, *22* (3), 898−905.

(7) Xu, N.; Liu, J.; Qiao, J.; Huang, H.; Zhou, X. D. Interweaving between MnO_2 Nanowires/ Nanorods and Carbon Nanotubes as Robust Multifunctional Electrode for Both Liquid and Flexible Electrochemical Energy Devices. *J. Power Sources* **2020**, *455*, 227992.

(8) Wang, F.; Zheng, Y.; Chen, Q.; Yan, Z.; Lan, D.; Lester, E.; Wu, T. A Critical Review of Facets and Defects in Different MnO_2 Crystalline Phases and Controlled Synthesis − Its Properties and Applications in the Energy Field. *Coord. Chem. Rev.* **2024**, *500*, 215537.

(9) Roche, I.; Chaînet, E.; Chatenet, M.; Vondrák, J. Carbon-Supported Manganese Oxide Nanoparticles as Electrocatalysts for the Oxygen Reduction Reaction (ORR) in Alkaline Medium: Physical Characterizations and ORR Mechanism. *J. Phys. Chem. C* **2007**, *111* (3), 1434−1443.

(10) Fink, M. F.; Weiss, M.; Marschall, R.; Roth, C. Experimental Correlation of Mn^{3+} Cation Defects and Electrocatalytic Activity of α-MnO_2 - an X-Ray Photoelectron Spectroscopy Study. *J. Mater. Chem. A* **2022**, *10* (29), 15811−15838.

(11) Lan, B.; Zheng, X.; Cheng, G.; Han, J.; Li, W.; Sun, M.; Yu, L. The Art of Balance: Engineering of Structure Defects and Electrical Conductivity of α-MnO_2 for Oxygen Reduction Reaction. *Electrochim. Acta* **2018**, *283*, 459−466.

(12) Davis, D. J.; Lambert, T. N.; Vigil, J. A.; Rodriguez, M. A.; Brumbach, M. T.; Coker, E. N.; Limmer, S. J. Role of Cu-Ion Doping in Cu-α-MnO_2 Nanowire Electrocatalysts for the Oxygen Reduction Reaction. *J. Phys. Chem. C* **2014**, *118* (31), 17342−17350.

(13) Suntivich, J.; Gasteiger, H. A.; Yabuuchi, N.; Nakanishi, H.; Goodenough, J. B.; Shao-Horn, Y. Design Principles for Oxygen-Reduction Activity on Perovskite Oxide Catalysts for Fuel Cells and Metal-Air Batteries. *Nat. Chem.* **2011**, *3* (7), 546−550.

(14) Rampf, A.; Leiter, R.; Fleischmann, S.; Elia, G. A.; Zeis, R. Tailoring α-MnO_2 Gas Diffusion Electrodes for Enhanced Oxygen Reduction in Aluminum-Air Batteries. *J. Energy Chem.* **2026**, *114*, 473−484.

(15) Ohma, A.; Shinohara, K.; Iiyama, A.; Yoshida, T.; Daimaru, A. Membrane and Catalyst Performance Targets for Automotive Fuel Cells by FCCJ Membrane, Catalyst. *MEA WG. ECS Trans.* **2011**, *41* (1), 775−784.

(16) Ji, S. G.; Kim, H.; Lee, W. H.; Oh, H. S.; Choi, C. H. Real-Time Monitoring of Electrochemical Carbon Corrosion in Alkaline Media. *J. Mater. Chem. A* **2021**, *9* (35), 19834−19839.

(17) Roche, I.; Chaînet, E.; Chatenet, M.; Vondrák, J. Durability of Carbon-Supported Manganese Oxide Nanoparticles for the Oxygen Reduction Reaction (ORR) in Alkaline Medium. *J. Appl. Electrochem.* **2008**, *38* (9), 1195−1201.

(18) Speck, F. D.; Santori, P. G.; Jaouen, F.; Cherevko, S. Mechanisms of Manganese Oxide Electrocatalysts Degradation during Oxygen Reduction and Oxygen Evolution Reactions. *J. Phys. Chem. C* **2019**, *123* (41), 25267−25277.

(19) Bozzini, B.; Alleva, A.; Bonanni, V.; Ciancio, R.; Kourousias, G.; Guzzi, F.; Rajak, P.; Gianoncelli, A. Degradation of α-MnO_2 in Zn-Air Battery Gas-Diffusion Electrodes: An Investigation Based on Chemical-State Mapping. *Electrochim. Acta* **2025**, *513*, 145534.

(20) Marini, E.; Liebert, M.; Rossi, F.; De Souza, D. O.; Baumli, P.; Aquilanti, G.; Regnet, F.; Lüdeking, I.; Bozzini, B.; Jörissen, L.; Brimaud, S. Mapping of the Degradation Processes at Bifunctional O_2 Gas Diffusion Electrode for Aqueous Alkaline Metal-Air Batteries. *J. Power Sources* **2022**, *546*, 231879.

(21) Bekisch, A.; Skadell, K.; Ast, J.; Schulz, M.; Weidl, R.; Christiansen, S.; Stelter, M. Alternative Gas Diffusion Electrode Designs: Influence of Porosity Gradients on the Electrochemical Activity. *Adv. Energy Sustainable Res.* **2025**, *6* (4), 2400202.

(22) Bekisch, A.; Skadell, K.; Poppitz, D.; Schulz, M.; Weidl, R.; Stelter, M. Hydrophobic, Carbon Free Gas Diffusion Electrode for Alkaline Applications. *J. Electrochem. Soc.* **2020**, *167* (14), 144502.

(23) Ku, Y. P.; Ehelebe, K.; Hutzler, A.; Bierling, M.; Böhm, T.; Zitolo, A.; Vorokhta, M.; Bibent, N.; Speck, F. D.; Seeberger, D.; Khalakhan, I.; Mayrhofer, K. J. J.; Thiele, S.; Jaouen, F.; Cherevko, S. Oxygen Reduction Reaction in Alkaline Media Causes Iron Leaching from Fe-N-C Electrocatalysts. *J. Am. Chem. Soc.* **2022**, *144* (22), 9753−9763.

(24) Ishiki, N. A.; Teixeira Santos, K.; Bibent, N.; Kumar, K.; Reichmann, I.; Ku, Y. P.; Asset, T.; Dubau, L.; Mermoux, M.; Ge, H.; Berthon-Fabry, S.; Saveleva, V. A.; Paidi, V. K.; Glatzel, P.; Zitolo, A.; Mineva, T.; Guesmi, H.; Cherevko, S.; Ticianelli, E. A.; Maillard, F.; Jaouen, F. Evidence for the Stabilization of FeN_4 Sites by Pt Particles during Acidic Oxygen Reduction. *Nat. Commun.* **2025**, *16* (1), 6404.

(25) Zhang, H.; Osmieri, L.; Park, J. H.; Chung, H. T.; Cullen, D. A.; Neyerlin, K. C.; Myers, D. J.; Zelenay, P. Standardized Protocols for Evaluating Platinum Group Metal-Free Oxygen Reduction Reaction Electrocatalysts in Polymer Electrolyte Fuel Cells. *Nat. Catal.* **2022**, *5* (5), 455−462.

(26) Roiron, C.; Martin, V.; Kumar, K.; Dubau, L.; Maillard, F. Assessing Pt and Ni Dissolution Mechanism and Kinetics of Shape-Controlled Oxygen Reduction Nanocatalysts. *Electrochim. Acta* **2024**, *477*, 143760.

(27) Abbou, S.; Chattot, R.; Martin, V.; Claudel, F.; Solà-Hernandez, L.; Beauger, C.; Dubau, L.; Maillard, F. Manipulating the Corrosion Resistance of SnO_2 Aerogels through Doping for Efficient and

Downloaded from pubs.acs.org/acscatsci/article-pdf/doi/10.1021/acscatal.6c06787/6916174/cs-2026-06787e.pdf by KIT BIBLIOTHEK user on 16 November 2026

Durable Oxygen Evolution Reaction Electrocatalysis in Acidic Media. *ACS Catal.* **2020**, *10* (13), 7283−7294.
(28) Xu, C.; Herrmann, N.; Liu, X.; Horstmann, B.; Passerini, S. Addressing the Voltage and Energy Fading of Al-Air Batteries to Enable Seasonal/Annual Energy Storage. *J. Power Sources* **2023**, *574*, 233172.
(29) Assumpção, M. H. M. T.; De Souza, R. F. B.; Rascio, D. C.; Silva, J. C. M.; Calegaro, M. L.; Gaubeur, I.; Paixão, T. R. L. C.; Hammer, P.; Lanza, M. R. V.; Santos, M. C. A Comparative Study of the Electrogeneration of Hydrogen Peroxide Using Vulcan and Printex Carbon Supports. *Carbon N. Y.* **2011**, *49* (8), 2842−2851.
(30) Erbe, A.; Tesch, M. F.; Rüdiger, O.; Kaiser, B.; DeBeer, S.; Rabe, M. Operando Studies of Mn Oxide Based Electrocatalysts for the Oxygen Evolution Reaction. *Phys. Chem. Chem. Phys.* **2023**, *25* (40), 26958−26971.
(31) Pourbaix, M.; Atlas of Electrochemical Equilibria in Aqueous Solutions; Franklin, J. A., Translator National Association of Corrosion Engineers: Houston, Texas, USA, **1974**.
(32) Kozawa, A.; Kalnoki-Kis, T.; Yeager, J. F. Solubilities of Mn(Ll) and Mn(Lll) Ions in Concentrated Alkaline Solutions. *J. Electrochem. Soc.* **1966**, *113* (5), 405−409.
(33) Qian, A.; Zhang, W.; Shi, C.; Pan, C.; Giammar, D. E.; Yuan, S.; Zhang, H.; Wang, Z. Geochemical Stability of Dissolved Mn(III) in the Presence of Pyrophosphate as a Model Ligand: Complexation and Disproportionation. *Environ. Sci. Technol.* **2019**, *53* (10), 5768−5777.
(34) Han, Z.; Roslie, H.; Tan, S. F.; Wu, D. Quasi-in Situ Observation of MnO_2 Nanorods by Electrochemical Transmission Electron Microscopy for Oxygen Reduction Reaction Process. *Adv. Energy Sustainability Res.* **2024**, *5* (6), 2300229.
(35) Tseng, L. T.; Lu, Y.; Fan, H. M.; Wang, Y.; Luo, X.; Liu, T.; Munroe, P.; Li, S.; Yi, J. Magnetic Properties in α-MnO_2 Doped with Alkaline Elements. *Sci. Rep.* **2015**, *5*, 9094.
(36) Yang, Z.; Ford, D. C.; Park, J. S.; Ren, Y.; Kim, S.; Kim, H.; Fister, T. T.; Chan, M. K. Y. Probing the Release and Uptake of Water in A-MnO_2·xH_2O. *Chem. Mater.* **2017**, *29* (4), 1507−1517.
(37) Kumar, K.; Dubau, L.; Jaouen, F.; Maillard, F. Review on the Degradation Mechanisms of Metal-N-C Catalysts for the Oxygen Reduction Reaction in Acid Electrolyte: Current Understanding and Mitigation Approaches. *Chem. Rev.* **2023**, *123* (15), 9265−9326.
(38) Wierzbicki, S.; Douglin, J. C.; Singh, R. K.; Dekel, D. R.; Kruczała, K. Operando EPR Study of Radical Formation in Anion-Exchange Membrane Fuel Cells. *ACS Catal.* **2023**, *13* (4), 2744−2750.
(39) Bae, G.; Chung, M. W.; Ji, S. G.; Jaouen, F.; Choi, C. H. pH Effect on the H_2O_2-Induced Deactivation of Fe-N-C Catalysts. *ACS Catal.* **2020**, *10* (15), 8485−8495.
(40) Guo, N.; Zhang, R.; Li, J.; Sun, Z.; Fei, T.; Sun, P. Impact of Aqueous Environments on Hydrogen Peroxide Activation by Manganese Oxides: Kinetics and the Critical Role of Bicarbonate. *Chemosphere* **2023**, *324*, 138338.
(41) Kanungo, S. B.; Parida, K. M.; Sant, B. R.; Studies on MnO_2—III. The Kinetics and the Mechanism for the Catalytic Decomposition of H_2O_2 over Different Crystalline Modifications of MnO_2. *Electrochim. Acta* **1981**, *26* (8), 1157−1167.
(42) Speck, F. D.; Zagalskaya, A.; Alexandrov, V.; Cherevko, S. Periodicity in the Electrochemical Dissolution of Transition Metals. *Angew. Chem., Int. Ed.* **2021**, *60* (24), 13343−13349.
(43) Lima, F. H. B.; Calegaro, M. L.; Ticianelli, E. A. Electrocatalytic Activity of Manganese Oxides Prepared by Thermal Decomposition for Oxygen Reduction. *Electrochim. Acta* **2007**, *52* (11), 3732−3738.
(44) Mao, L.; Zhang, D.; Sotomura, T.; Nakatsu, K.; Koshiba, N.; Ohsaka, T. Mechanistic Study of the Reduction of Oxygen in Air Electrode with Manganese Oxides as Electrocatalysts. *Electrochim. Acta* **2003**, *48* (8), 1015−1021.
(45) Cao, Y. L.; Yang, H. X.; Ai, X. P.; Xiao, L. F. The Mechanism of Oxygen Reduction on MnO_2-Catalyzed Air Cathode in Alkaline Solution. *J. Electroanal. Chem.* **2003**, *557*, 127−134.
(46) Lide, D. R. *CRC Handbook of Chemistry and Physics*; CRC Press: Boca Raton, FL, **2006**.
(47) Rabe, M.; Toparli, C.; Chen, Y. H.; Kasian, O.; Mayrhofer, K. J. J.; Erbe, A. Alkaline Manganese Electrochemistry Studied by in Situ and Operando Spectroscopic Methods - Metal Dissolution, Oxide Formation and Oxygen Evolution. *Phys. Chem. Chem. Phys.* **2019**, *21* (20), 10457−10469.
(48) Antxustegi, M. M.; Pierna, A. R.; Ruiz, N. Chemical Activation of Vulcan® XC72R to Be Used as Support for NiNbPtRu Catalysts in PEM Fuel Cells. *Int. J. Hydrogen Energy* **2014**, *39* (8), 3978−3983.
(49) Rittiruam, M.; Buapin, P.; Saelee, T.; Khajondetchairit, P.; Kheawhom, S.; Alling, B.; Praserthdam, S.; Ektarawong, A.; Praserthdam, P. First-Principles Calculation on Effects of Oxygen Vacancy on α-MnO_2 and β-MnO_2 during Oxygen Reduction Reaction for Rechargeable Metal-Air Batteries. *J. Alloys Compd.* **2022**, *926*, 166929.
(50) Qiao, J.; Xu, L.; Ding, L.; Shi, P.; Zhang, L.; Baker, R.; Zhang, J. Effect of KOH Concentration on the Oxygen Reduction Kinetics Catalyzed by Heat-Treated Co-Pyridine/C Electrocatalysts. *Int. J. Electrochem. Sci.* **2013**, *8*, 1189−1208.
(51) Yu, H. Y.; Li, X. F.; Zhang, T. H.; Liu, J.; Tian, J. H.; Yang, R. Oxygen Reduction Reaction on Au Revisited at Different PH Values Using in Situ Surface-Enhanced Raman Spectroscopy. *ChemSusChem* **2020**, *13* (10), 2702−2708.
(52) Hamada, A. T.; Orhan, M. F.; Kannan, A. M. Alkaline Fuel Cells: Status and Prospects. *Energy Rep.* **2023**, *9*, 6396−6418.
(53) Ding, X.; Luo, D.; Cui, J.; Xie, H.; Ren, Q.; Lin, Z. An Ultra-Long-Life Lithium-Rich $Li_{1.2}Mn_{0.6}Ni_{0.2}O_2$ Cathode by Three-in-One Surface Modification for Lithium-Ion Batteries. *Angew. Chem., Int. Ed.* **2020**, *59* (20), 7778−7782.
(54) Wang, Y.; Liu, J.; Yuan, H.; Liu, F.; Hu, T.; Yang, B. Strong Electronic Interaction between Amorphous MnO_2 Nanosheets and Ultrafine Pd Nanoparticles toward Enhanced Oxygen Reduction and Ethylene Glycol Oxidation Reactions. *Adv. Funct. Mater.* **2023**, *33* (21), 2211909.
(55) Ke, Q.; Zhang, Y.; Wan, C.; Tang, J.; Li, S.; Guo, X.; Han, M.; Hamada, T.; Osman, S. M.; Kang, Y.; Yamauchi, Y. Sunlight-Driven and Gram-Scale Vanillin Production via Mn-Defected γ-MnO_2 Catalyst in Aqueous Environment. *Chem. Sci.* **2024**, *15* (14), 5368−5375.
(56) Housel, L. M.; Wang, L.; Abraham, A.; Huang, J.; Renderos, G. D.; Quilty, C. D.; Brady, A. B.; Marschilok, A. C.; Takeuchi, K. J.; Takeuchi, E. S. Investigation of α-MnO_2 Tunneled Structures as Model Cation Hosts for Energy Storage. *Acc. Chem. Res.* **2018**, *51*(3), 575−582.

Downloaded from pubs.acs.org/acscatsci/article-pdf/doi/10.1021/acscatal.6c06787/6916174/cs-2026-06787e.pdf by KIT BIBLIOTHEK user on 16 November 2026

https://doi.org/10.1021/acscatal.6c06787
ACS Catal. XXXX, XXX, XXX−XXX